Designing tough isotropic structural composite using computation, 3D printing and testing

Yongtae Kim[1], Youngsoo Kim[1], Flavia Libonati[2**], and Seunghwa Ryu[1,*]

Affiliations

[1] Department of Mechanical Engineering, Korea Advanced Institute of Science and Technology (KAIST), 291 Daehak-ro, Yuseong-gu, Daejeon 34141, Republic of Korea

[2] Department of Mechanical Engineering, Politecnico di Milano, Milan, Italy

[*]Corresponding author e-mail: ryush@kaist.ac.kr

[**]Co-corresponding author e-mail: flavia.libonati@polimi.it

Keywords
Isotropic structural composite; toughening mechanism; 3D printing

Abstract

Staggered platelet composites found in nature, such as nacre, bone, and conch-shell, exhibit a remarkable combination of high toughness, strength, and stiffness, and have inspired the development of bio-inspired composites mimicking their characteristic features. However, those excellent mechanical properties are primarily observed under specific loading conditions due to their mechanical anisotropy, which originates from the aligned microstructures consisting of high aspect ratio inclusions. In this study, we combine numerical simulations and 3D-printing to propose a design strategy of isotropic two-dimensional structural composites consisting of stiff and soft constituents that are arranged in square, triangular, and quasicrystal lattices. For these relatively isotropic structures, the soft tile/stiff boundary configuration significantly outperforms the stiff tile/soft boundary configuration in terms of normalized toughness, strength, and stiffness with respect to the simple rule of mixture estimates for each, because the former provides more extrinsic toughening mechanisms and effectively lower the stress concentration near the crack tip. The quasicrystal lattice offers the best isotropy in elastic response, while its absolute values of stiffness, strength, and toughness turn out to be similar or lower than those of triangular lattice composites due to more irregular stress distribution. In contrast, for the highly anisotropic staggered platelet structure, the stiff tile/soft boundary configuration significantly outperforms the inverted one, owing to its unique load-transfer mechanism which relies primarily on the shear-lag effect.

1. Introduction

Inspired by natural load-bearing materials, significant efforts have been devoted to obtaining optimal structural composites exhibiting high strength and toughness at the same time [1-5], while avoiding the limitation of most engineering materials, a mutually exclusive relationship between strength and toughness [6]. Many natural organisms achieve the strength-toughness balance by evolving their body composition into composites consisting of both stiff and soft constituents in specific arrangements that are optimized to resist certain loading conditions from the environment and natural enemies [7-12]. Such a need has led most natural structural materials to have significantly anisotropic mechanical properties, which are excellent against some loading conditions at the expense of inferior responses under other loading conditions [11, 13-16]. For instance, nacre, which is composed of 95% of high aspect ratio stiff mineralized aragonite and 5% of soft biological polymer in a staggered platelet structure, shows excellent strength and toughness under tension in the longitudinal direction (i.e. parallel to the longitudinal platelet axis) because of the unique inter-lamellae slip mechanism of the stiff aragonite platelets stacked with the soft organic materials [7, 10-12, 15, 17, 18]. However, such mechanism does not operate under tension along the transversal direction, which results in very weak mechanical resistance [7, 19, 20]. Similarly, the anisotropic nanostructure of bone, which consists of mineralized cylindrical collagen fibrils stacked in an extrafibrillar matrix (mainly made of soft collagen molecules) results in very anisotropic mechanical properties [11, 14, 16, 21]. Accordingly, bio-inspired composites that mimic the microstructures of such natural composites exhibit very strong anisotropy in mechanical responses [22-25].

Despite the presence of mechanically isotropic natural materials and the need for constructing composites with better isotropic responses [18, 26], relatively less attention has been paid to the design of mechanically isotropic composites. Most existing studies have mainly focused on understanding and strengthening the mechanical properties in specific directions with additional toughening mechanisms, such as mineral bridges and wavy interlocking shaped platelets in the out-of-plane direction [27, 28]. The effect of inclusion aspect ratio has been investigated in studies considering osteon-like composites [23, 24], albeit the primary focus was not on the design of isotropic composites.

In this study, we investigate a design strategy of two-dimensional structural composites that possess both excellent mechanical properties and high degree of isotropy. We consider composites made of stiff and soft phases to enhance toughness by leveraging the extrinsic toughening mechanisms that originate from crack deviation and stress delocalization. To construct composites with reduced loading direction dependence, we consider the composites arranged in relatively isotropic two-dimensional Bravais lattices (square and triangular), as well as quasicrystal lattice. For the triangular lattice, we consider two types of unit cells with either circular or hexagonal tiles to preserve the six-fold rotational symmetry of the triangular lattice. Also, inspired by the previous studies of one of the authors [23, 24], we consider two configurations, soft-tile/stiff-boundary (SoTStB) and stiff-tile/soft-boundary (StTSoB), with fixed tile/boundary volume fraction, as illustrated in Figure 1. We compare the absolute values and isotropies of stiffness, strength, and toughness for the eight composite structures, by employing numerical simulations based on the spring network model, and experimental testing carried out on 3D-printed samples. We also discuss the performance of SoTStB and StTSoB configurations for the highly anisotropic staggered platelet structure mimicking nacre, to highlight the difference between isotropic and anisotropic structures.

2. Methodology

2.1 Construction of two-dimensional isotropic composite structure

The structural composites were constructed in square, triangular, and quasicrystal lattices, composed of soft and stiff materials, as represented by the grey and black regions, respectively (Figure 1). The square lattice and triangular (or hexagonal) lattice were chosen because they have four-fold and six-fold rotational symmetries, respectively, while the other three two-dimensional Bravais lattices have only two-fold rotational symmetry [29]. For the triangular lattice, we consider two different unit cells made of circular and hexagonal tiles, which preserve the six-fold symmetry in elastic moduli [30, 31]. The triangular lattice with circular tile has been previously studied for a bone-inspired composite mimicking the Harversian structure [23, 24].

We also adopted a quasicrystal structure, called Penrose tiling, which lacks both translational and rotational symmetry, as highlighted in a view overlapped with the translated Penrose tiling in Figure 2a: as a result, the elastic response becomes isotropic when averaged over sufficiently large numbers of quasi-unit cells [32]. Hereafter, we will refer to the square lattice with square tiles as the 'square structure', the triangular lattice with circular tiles as the 'circle structure', the triangular lattice with hexagonal tiles as the 'hexagon structure', and the quasicrystal lattice based on Penrose tiling as the 'quasicrystal structure'. To make a fair comparison among the four structures, we used an identical unit cell area for all the structures (see details defining the equivalent unit cell for Penrose tiling in Figure S1, Supplementary Information), and an identical areal ratio of tile (around 63%), inspired by the previous studies on the bone-inspired composite mimicking the Harversian structure [23, 24].

We measured the anisotropies of mechanical properties such as stiffness, strength, toughness, and fracture strain by considering the relative difference in the maximum and minimum values measured along tension in different directions. Due to the four-fold symmetry, the square structure is expected to exhibit two extreme mechanical responses under uniaxial tension, along $\theta = 0°$ and $\theta = 45°$ orientations, as depicted in Figure 1. θ

refers to the counter-clockwise rotational angle relative to the reference configuration in the 1st column of Figure 1. Circle and hexagon structures will have two extreme mechanical responses, from $\theta = 0°$ and $\theta = 90°$ orientations, due to the six-fold symmetry. For the quasicrystal structure featuring five-fold local symmetry, we considered four representative orientations, with rotation angles of $\theta = 0°, 45°, 90°$, and $135°$. These rotation angles were chosen to minimize artifacts from the inherent 8-fold rotational symmetry of the mechanical properties of the bead-spring network model used in the study (see details in the Supplementary Information).

2.2 Simulation methods using sLSM (square Lattice Spring Model)

For the numerical simulations of tensile loading, we employed the bead-spring model, also known as the lattice spring model (LSM), to analyze the deformation/fracture mechanism of the structural materials. We underline that the word ‘lattice’ in lattice spring model means “bead-spring network”, adopted for the material discretization (Figure 2b), and is different from the lattice defining the arrangements of stiff and soft constituents in the previous section. Because of its computational efficiency and ease of implementation, LSM has been used to analyze the deformation and fracture mechanism of nature-inspired composites [24, 33-40]. However, most previous studies have employed triangular LSM (tLSM), where mechanical properties highly depend on the loading direction [24, 33-39]. The inherent anisotropy of the spring network was less concerning when modeling those highly anisotropic composites because its primary purpose is to capture the toughening mechanism in a qualitative manner. However, it becomes a more important issue when studying the isotropy of composites. Hence, in this study, we adopted square LSM (sLSM), which is known to have a reduced anisotropy in elastic behavior and a reduced anisotropy in fracture behavior, allowing us to more selectively consider the effect of macroscopic stiff/soft-phases arrangements [41]. Detailed information about the sLSM used in the study is described in the Supplementary Information.

For the numerical simulations with sLSM, we employed the large-scale atomic/molecular massively parallel simulator (LAMMPS) package [42]. To simulate two different material phases, the spring constant for the stiff material region was specified to be 100 times larger than that of soft materials, and the spring cut-off values for the soft material region were set to assign equivalent toughness modulus to the stiff and soft materials, as indicated in Table 1. We set around 400 beads per unit cell to minimize the size effect as well as the artifact in the discretization [36]. The overall size of the samples was chosen to be about 800 horizontal spring segments in both the x and y directions.

We considered a single edge-notched sample with a pre-existing crack spanning 20% of the sample width, as shown in Figure 2. The pre-existing crack was modelled by removing the springs along the crack, and the crack tip was positioned at the center of a tile to allow some spacing from the boundary. We conducted quasi-static uniaxial tension simulations by applying an incremental strain of 2.5×10^{-4} via an affine transformation and running energy minimization with the conjugate gradient method. This procedure was repeated until the samples were fully fractured. Stress distribution was obtained using the Virial stress definition, which is equivalent to the Cauchy stress for quasi-static loading at 0K [43].

2.3 Experimental methods with 3D-printed structures

Experimental testing was performed on composites fabricated via multi-material 3D-printing. We adopted the Stratasys J750, a PolyJet printer making complex geometry by spraying liquid layers of the photopolymer precursors, which are subsequently solidified by UV light [44]. This technology ensures good interfacial adhesion between the two different materials [23, 34]. Hence, experimental validation can be performed by ignoring the weak interfacial bonding problem. However, at the same time, the intermixing of different liquid precursors before curing causes printing direction-dependent mechanical properties in the materials [45, 46].

In this study, to minimize the anisotropy caused by the printing direction dependency, we used an equivalent printing direction for all the samples as depicted in the Supplementary Information. As with the simulations, we assigned an equivalent size to the periodic (or quasi-periodic) unit cell of each structure. The samples are notched at 20% of their length, and the crack tips are placed at the center of the tile. We designated the stiff materials as VeroWhitePlus and the soft material as DM9875, to ensure a high enough modulus ratio between the soft and stiff phases. The material properties of the notched base material samples are presented in Table S1. In the 3D-printed samples, the volume fraction of materials occupying the tile region of each composites was set to be $64 \pm 0.2\%$, which is almost identical to that of the simulations.

To measure the mechanical properties of both the base materials and the composites, we conducted tensile experiments with an MTS alliance RT/100 Universal Testing Machine having 100kN load cell. In order to apply tensile deformation, the samples were clamped with a thickened grip part made of stiff materials, and displacement control was applied. To limit the viscoelastic effect on the mechanical response of the base materials, we used a slow strain rate, 0.01/min, applied through a crosshead speed of 0.7 mm/min and gauge length of 70 mm. The overall specimen dimensions are represented in Figure S8 of Supplementary Information.

Results and discussion

3.1 Stress distribution and fracture mechanism of the SoTStB/StTSoB composite observed in the simulations

Figure 3 compares the stress distribution of a homogeneous stiff sample (Fig 3a) with those of SoTStB (Fig 3b) and StTSoB (Fig 3c) with $\theta = 0°$ subjected to the uniaxial strain of $\varepsilon_{xx} = 0.001$. The stress distributions (σ_{xx} component) were visualized by the Open Visualization Tool (OVITO) [47]: the red and navy colors represent the maximum and minimum stresses, respectively. The units of stresses are represented with the spring constants (k) and the undeformed axial spring length (r_0) of the sLSM.

For the homogeneous sample and the StTSoB samples, the stress was highly concentrated at the crack tip. In contrast, the SoTStB samples not only showed significantly reduced stress concentration at the crack tip, but also a more heterogeneous stress distribution over the entire volume. We found that such heterogeneous stress distribution promotes the activation of additional toughening mechanisms, such as uncracked-ligament bridging and constrained microcracking. For the SoTStB samples (Figure 4a), microcracks formed in front of the primary crack tip during the fracture process, promoting additional energy dissipation, and the interaction between microcracks and primary crack led to wavy crack propagations. In addition, the crack-bridging mechanism induced by the stiff boundary segments contributed to a further increase in toughness [14]. These findings, also observed in the bone-inspired topology, here called circular structure, are corroborated by previous studies on bone tissues, which revealed that the heterogeneity in bone structure plays a crucial role in increasing flaw tolerance, promoting strain delocalization, and boosting energy dissipation during deformation and failure [48, 49]. Contrarily, the cracks in the homogeneous sample and the StTSoB samples propagated continuously along the soft boundary until the complete failure because of the high stress concentration at the crack tip, as shown in Figure 4b.

3.2 Comparison between the SoTStB and StTSoB samples

We obtained the stiffness, toughness, fracture strength, and fracture strain from the stress strain curves of single-edge notched samples (Figure 5). The stiffness was obtained from the initial slope, toughness and fracture strength were defined by the area underneath the stress-strain curve until complete fracture and the maximum stress, respectively. The fracture strain was defined as the strain at which the stress is reduced by 95 % of the maximum stress, to filter out artifacts from the numerical error, i.e., the small post-fracture stress fluctuation that occurs from a few remaining spring segments.

The maximum and minimum mechanical properties of each composite structure are illustrated in Figure 6. The toughness of the SoTStB composites is significantly higher than that of StTSoB composites, which can be explained by two primary reasons. First, the stress required to initiate crack propagation in SoTStB composite is greater than that needed by the StTSoB composites, because the stress concentration at the crack tip is delocalized in the SoTStB composites. Second, the activation of extrinsic toughening mechanisms during crack propagation in the SoTStB composites contributes to a higher energy dissipation. This can be confirmed by the gradual stress reduction after the fracture initiation of SoTStB in Figure 5. The mechanism observed in the SoTStB composites is different from that of the conventional anisotropic staggered platelet composites with the StTSoB configuration, where the primary toughening mechanism is the crack detouring around the high aspect ratio stiff platelets [11]. We will discuss about the aspect ratio effect further in Section 3.4.

Additionally, although the volume fraction of the stiff phase in SoTStB (~ 37%) is much smaller than that of StTSoB (~ 63%), the stiffness and fracture strength values of the

SoTStB samples are higher than those of the StTSoB samples. This means that the microstructure has a larger contribution in defining the overall mechanical performance, than the averaged properties of the two constituents by simple rule of mixture.

For both the SoTStB and StTSoB samples, the percolated boundary phase is responsible for the primary load transfer mechanism under tension. As an extreme example, the square structure under tension along $\theta = 0^\circ$ sustains the external loading primarily via the tensile elongation of two kinds of parallel entities: the thin boundary phase line and thick alternating boundary-tile strip. The stiffness can be roughly estimated from the Voigt rule of mixture of the two parallel entities [50], and one can notice that it is advantageous to dispatch stiff materials in the percolated continuous boundary line for efficient load transfer. Like cellular solids, the stiff materials aligned along the tensile direction are subjected to stretching-dominant deformation, requiring larger strain energy than the bending-dominant deformation [51]. Hence, despite a significantly smaller fraction of stiff phase in SoTStB, the maximum stiffness of the SoTStB square structure was significantly higher than the maximum stiffness of StTSoB counterpart.

Although the load transfer mechanisms in the other structures (circle, hexagon, quasicrystal structures) were more complex, it is evident that the percolating stiff boundary phase is responsible for the efficient load transfer mechanism in SoTStB. Accordingly, the fracture strength of SoTStB was predominantly higher than that of StTSoB samples. These findings also show there are some similarities between the SoTStB structures in this study and cortical bone tissue, where the osteons are interspersed into a more mineralized (i.e. stiffer) matrix, and could provide further insights into the deformation and toughening mechanisms occurring in bone Haversian structure.

3.3 Comparison of the different geometrical structures of SoTStB samples

After showing that the SoTStB exhibited superior mechanical properties compared to StTSoB, we turned our attention to evaluating the effect of different geometrical structures in SoTStB configurations. As shown in Figure 5, the anisotropy of the square lattice was the largest because the deformation and fracture mechanisms are completely different for each loading direction. The stiff boundary phase undergoes stretching-dominant deformation for $\theta = 0°$ tension requiring large strain energy, while it undergoes bending-dominant deformation for the $\theta = 45°$ tension requiring much less strain energy, as presented in Figure 7. In comparison, a combination of stretching and bending deformation occurs in tensile loading along any direction for the other three structures (circle, hexagon, and quasicrystal), leading to a significantly higher degree of isotropy. Due to the lack of long-range translational order and rotational symmetry, the quasicrystal structure shows the most isotropic response in the elastic regime, i.e. stiffness (Figure 6). The circle structure has noticeably higher stiffness and strength compared to hexagon and quasicrystal structures, because its percolated boundary has rounder junction, which induces less stress concentration and thus endows higher resistance to the bending deformation. Because the fracture strength is determined by the crack growth at the weakest point (either with the highest stress concentration and/or weakest material property) out of the entire specimen, the quasicrystal sample is likely to undergo an earlier crack nucleation/initiation compared to the hexagon or the circle structure under identical loading because it possesses the most heterogeneous stress distribution (or, highest standard deviation of stress). Still, because the heterogeneous stress distribution promotes external toughening mechanisms, the toughness modulus is comparable to circle or hexagon structures.

After numerically predicting the mechanical properties of the various composite designs, we tested the SoTStB prototypes fabricated with the multimaterial 3D-printer. The outcomes of the tests are depicted in Figure 8. Both the numerical and experimental results show that the circle structure has relatively higher stiffness compared to the others, and the quasicrystal structure exhibits the most isotropic elastic response. The experimental results qualitatively agree with the numerical ones, but not quantitatively. This can be attributed to: i) the stress-strain curve of the soft constituent materials in experiments is nonlinear while in the numerical modeling it is assumed to be linear until fracture, ii) the intermixing of liquid precursors at the stiff/soft material interface causes the printing-orientation-dependent material properties, and iii) the artifacts of the discrete LSM model in simulations, iv) the different ratios of mechanical properties between the stiff and soft phases in experiments and simulations. Still, we note that the LSM-based design can be used as a guideline to qualitatively predict the mechanical performance of different composite structures.

3.4 Comparison of the anisotropic staggered platelet structures of SoTStB and StTSoB

We have shown that the SoTStB structures outperform StTSoB ones for isotropic composites. Now, to better highlight the role of structural anisotropy, we turn our attention to the performance of SoTStB and StTSoB for staggered platelet structures in a brick and mortar style. We constructed the staggered platelet structures with a rectangular tile having an aspect ratio of ~12, which is similar to the aspect ratio of platelets in nacre [52], as depicted in Figure 9 (a). The stress distributions under uniaxial tension are plotted in Figure 9 (b). The anisotropic brick-and-mortar StTSoB composite has a lower stress concentration at the crack tip compared to the isotropic StTSoB composites (Figure 3c), because the load transfer via the inter-lamellar slip (or shear-lag effect) becomes significant. Accordingly, the crack path increases significantly due to the crack-detouring, enhancing the toughness, as shown in Figure 9c,d. Compared to the properties of the isotropic square StTSoB structure with the same volume fraction, the toughness, fracture strength, stiffness, and fracture strain are improved multiple times with the increase in tile aspect ratio. This effect has also been confirmed by research works on the natural brick-and-mortar structures, e.g. nacre and bone ultrastructure, where the stiff platelets carry the load and the soft matrix transfers the load by shear, and helps dissipate the energy.

In contrast, for the SoTStB composite, the stiffness and fracture strength are relatively constant values, regardless of the tile aspect ratio (Figure 9d and Figure 5). The stress distribution of the highly anisotropic SoTStB composite (Figure 9b) is similar to that of the square SoTStB composite (Figure 3c) and the crack path is also similar (Figure 9c and Figure 4b) owing to the similarity in the load transfer mechanism. The stretching of the percolated stiff boundary is the primary load transfer mechanism occurring in both the anisotropic and isotropic SoTStB structures, regardless of the aspect ratio or overlap between the tiles.

Conclusion

In this work, we investigate the mechanical properties of isotropic two-dimensional structural composites consisting of stiff and soft constituents that are arranged in relatively isotropic structures involving small aspect ratio inclusions. We adopted a comprehensive approach, including numerical simulations, to provide the main design guidelines, and additive manufacturing as proof-of-concept. We find that the SoTStB configuration significantly outperforms the StTSoB configuration, because the former provides more extrinsic toughening mechanisms and effectively lower the stress concentration near the crack tip. We also reveal that the composite in a quasicrystal lattice shows the best isotropy in elastic response, while its absolute values of stiffness, strength, and toughness turn out to be similar or lower than those of the composites organized in triangular lattice. This structure dependency, observed in the numerical study, draws parallels to mechanisms and properties seen in the experiments with the four different SoTStB composites fabricated by the multimaterial 3D-printer. In contrast, for the highly anisotropic staggered platelet structure, the StTSoB configuration outperforms the SoTStB one, owing to its unique load-transfer mechanism which relies primarily on the shear-lag effect.

Our study suggests that isotropic composites balancing stiffness, strength, and toughness can be constructed with SoTStB configuration which resembles the bone Haversian structure. We also show that the design guideline for the isotropic composite must be opposite to the anisotropic composite in the staggered platelet structure where the inverted configuration (StTSoB) provides better mechanical properties.

Acknowledgements

This work is supported by the National Research Foundation of Korea (NRF) funded by the Ministry of Science and ICT (2016M3D1A1900038 and 2016R1C1B2011979).

References

1. Bouville, F., et al., *Strong, tough and stiff bioinspired ceramics from brittle constituents.* Nature materials, 2014. **13**(5): p. 508-514.
2. Wan, S., et al., *Nacre-inspired integrated strong and tough reduced graphene oxide–poly (acrylic acid) nanocomposites.* Nanoscale, 2016. **8**(10): p. 5649-5656.
3. Papkov, D., et al., *Simultaneously strong and tough ultrafine continuous nanofibers.* ACS nano, 2013. **7**(4): p. 3324-3331.
4. Wei, Y., et al., *Evading the strength–ductility trade-off dilemma in steel through gradient hierarchical nanotwins.* Nature communications, 2014. **5**.
5. Mirkhalaf, M., A.K. Dastjerdi, and F. Barthelat, *Overcoming the brittleness of glass through bio-inspiration and micro-architecture.* Nature communications, 2014. **5**.
6. Ritchie, R.O., *The conflicts between strength and toughness.* Nature materials, 2011. **10**(11): p. 817-822.
7. Sun, J. and B. Bhushan, *Hierarchical structure and mechanical properties of nacre: a review.* Rsc Advances, 2012. **2**(20): p. 7617-7632.
8. Rho, J.-Y., L. Kuhn-Spearing, and P. Zioupos, *Mechanical properties and the hierarchical structure of bone.* Medical engineering & physics, 1998. **20**(2): p. 92-102.
9. Currey, J.D., *Hierarchies in biomineral structures.* Science, 2005. **309**(5732): p. 253-254.
10. Barthelat, F., Z. Yin, and M.J. Buehler, *Structure and mechanics of interfaces in biological materials.* Nature Reviews Materials, 2016. **1**: p. 16007.
11. Wang, R. and H.S. Gupta, *Deformation and fracture mechanisms of bone and nacre.* Annual Review of Materials Research, 2011. **41**: p. 41-73.
12. Wang, R.Z., et al., *Deformation mechanisms in nacre.* Journal of Materials Research, 2001. **16**(9): p. 2485-2493.
13. Koester, K.J., J.W. Ager, and R.O. Ritchie, *The true toughness of human cortical bone measured with realistically short cracks.* Nature materials, 2008. **7**(8): p. 672-677.
14. Nalla, R.K., J.H. Kinney, and R.O. Ritchie, *Mechanistic fracture criteria for the failure of human cortical bone.* Nature materials, 2003. **2**(3): p. 164.
15. Kakisawa, H. and T. Sumitomo, *The toughening mechanism of nacre and structural materials inspired by nacre.* Science and technology of advanced materials, 2012. **12**(6): p. 064710.
16. Launey, M.E., M.J. Buehler, and R.O. Ritchie, *On the mechanistic origins of toughness in bone.* Annual review of materials research, 2010. **40**: p. 25-53.
17. Xia, S., et al., *Nanoasperity: structure origin of nacre-inspired nanocomposites.* ACS nano, 2015. **9**(2): p. 2167-2172.
18. Luz, G.M. and J.F. Mano, *Mineralized structures in nature: examples and inspirations for the design of new composite materials and biomaterials.* Composites Science and Technology, 2010. **70**(13): p. 1777-1788.
19. Meyers, M.A., et al., *Biological materials: structure and mechanical properties.* Progress in Materials Science, 2008. **53**(1): p. 1-206.
20. Barthelat, F. and H. Espinosa, *An experimental investigation of deformation and fracture of nacre–mother of pearl.* Experimental mechanics, 2007. **47**(3): p. 311-324.
21. Ritchie, R.O., M.J. Buehler, and P. Hansma, *Plasticity and toughness in bone.* 2009.
22. Wegst, U.G.K., et al., *Bioinspired structural materials.* Nature materials, 2015. **14**(1): p. 23-36.
23. Libonati, F., et al., *Bone-Inspired Materials by Design: Toughness Amplification Observed Using 3D Printing and Testing.* Advanced Engineering Materials, 2016. **18**(8): p. 1354-1363.
24. Libonati, F., et al., *A computational framework to predict failure and performance of bone-inspired materials.* ACS Biomaterials Science & Engineering, 2017.
25. Libonati, F., C. Colombo, and L. Vergani, *Design and characterization of a biomimetic composite inspired to human bone.* Fatigue & Fracture of Engineering Materials & Structures, 2014. **37**(7): p. 772-781.
26. Weiner, S., L. Addadi, and H.D. Wagner, *Materials design in biology.* Materials Science and Engineering:

C, 2000. **11**(1): p. 1-8.

27. Djumas, L., et al., *Enhanced mechanical performance of bio-inspired hybrid structures utilising topological interlocking geometry.* Scientific reports, 2016. **6**: p. 26706.
28. Gu, G.X., et al., *Printing nature: Unraveling the role of nacre's mineral bridges.* Journal of the mechanical behavior of biomedical materials, 2017. **76**: p. 135-144.
29. Kittel, C., P. McEuen, and P. McEuen, *Introduction to solid state physics*. Vol. 8. 1996: Wiley New York.
30. Christensen, R.M., *Sufficient symmetry conditions for isotropy of the elastic moduli tensor.* Journal of applied mechanics, 1987. **54**(4): p. 772-777.
31. Dresselhaus, M.S. and G. Dresselhaus, *Note on sufficient symmetry conditions for isotropy of the elastic moduli tensor.* Journal of Materials Research, 1991. **6**(5): p. 1114-1118.
32. Lifshitz, R., *The symmetry of quasiperiodic crystals.* Physica A: Statistical Mechanics and its Applications, 1996. **232**(3-4): p. 633-647.
33. Dimas, L.S. and M.J. Buehler, *Tough and stiff composites with simple building blocks.* Journal of Materials Research, 2013. **28**(10): p. 1295-1303.
34. Dimas, L.S., et al., *Tough composites inspired by mineralized natural materials: computation, 3D printing, and testing.* Advanced Functional Materials, 2013. **23**(36): p. 4629-4638.
35. Libonati, F. and M.J. Buehler, *Advanced Structural Materials by Bioinspiration.* Advanced Engineering Materials, 2017.
36. Dimas, L.S. and M.J. Buehler, *Influence of geometry on mechanical properties of bio-inspired silica-based hierarchical materials.* Bioinspiration & biomimetics, 2012. **7**(3): p. 036024.
37. Sen, D. and M.J. Buehler, *Structural hierarchies define toughness and defect-tolerance despite simple and mechanically inferior brittle building blocks.* Scientific reports, 2011. **1**: p. 35.
38. Dimas, L.S. and M.J. Buehler, *Modeling and additive manufacturing of bio-inspired composites with tunable fracture mechanical properties.* Soft Matter, 2014. **10**(25): p. 4436-4442.
39. Mirzaeifar, R., et al., *Defect-tolerant bioinspired hierarchical composites: simulation and experiment.* ACS Biomaterials Science & Engineering, 2015. **1**(5): p. 295-304.
40. Brely, L., F. Bosia, and N.M. Pugno, *A hierarchical lattice spring model to simulate the mechanics of 2-D materials-based composites.* Frontiers in Materials, 2015. **2**: p. 51.
41. Kim, Y., Y. Kim, and S. Ryu, *Elastic and fracture property analyses of triangular and square lattice spring models at a large deformation regime.* Journal of Mechanical Science and Technology, 2018. **32**(6): p. 2693-2706.
42. Plimpton, S., P. Crozier, and A. Thompson, *LAMMPS-large-scale atomic/molecular massively parallel simulator.* Sandia National Laboratories, 2007. **18**: p. 43-43.
43. Subramaniyan, A.K. and C. Sun, *Continuum interpretation of virial stress in molecular simulations.* International Journal of Solids and Structures, 2008. **45**(14-15): p. 4340-4346.
44. Lee, J.-Y., J. An, and C.K. Chua, *Fundamentals and applications of 3D printing for novel materials.* Applied Materials Today, 2017. **7**: p. 120-133.
45. Kim, Y., et al., *An Extended Analytic Model for the Elastic Properties of Platelet-Staggered Composites and Its Application to 3D Printed Structures.* Composite Structures, 2018.
46. Zhang, P. and A.C. To, *Transversely isotropic hyperelastic-viscoplastic model for glassy polymers with application to additive manufactured photopolymers.* International Journal of Plasticity, 2016. **80**: p. 56-74.
47. Stukowski, A., *Visualization and analysis of atomistic simulation data with OVITO–the Open Visualization Tool.* Modelling and Simulation in Materials Science and Engineering, 2009. **18**(1): p. 015012.
48. Tai, K., et al., *Nanoscale heterogeneity promotes energy dissipation in bone.* Nature materials, 2007. **6**(6): p. 454.
49. Yao, H., et al., *Size-dependent heterogeneity benefits the mechanical performance of bone.* Journal of the Mechanics and Physics of Solids, 2011. **59**(1): p. 64-74.
50. Voigt, W., *Ueber die Beziehung zwischen den beiden Elasticitätsconstanten isotroper Körper.* Annalen

der physik, 1889. **274**(12): p. 573-587.

51. Deshpande, V.S., M.F. Ashby, and N.A. Fleck, *Foam topology: bending versus stretching dominated architectures.* Acta materialia, 2001. **49**(6): p. 1035-1040.

52. Rabiei, R., S. Bekah, and F. Barthelat, *Failure mode transition in nacre and bone-like materials.* Acta biomaterialia, 2010. **6**(10): p. 4081-4089.

Tables

		Spring constant	Spring cut off length	Spring fracture energy
Stiff Materials	Axial spring	$1000k$	$1.01r_0$	$5\times 10^{-2}k$
	Diagonal spring	$500k$	$1.01\times \sqrt{2}r_0$	$5\times 10^{-2}k$
Soft materials	Axial spring	$10k$	$1.1r_0$	$5\times 10^{-2}k$
	Diagonal spring	$5k$	$1.1\times \sqrt{2}r_0$	$5\times 10^{-2}k$

Table 1. The spring properties assigned for the stiff/soft phase in the sLSM. r_0 represents the length between the nearest neighbor beads, which is unit lattice spacing. To model isotropic materials with sLSM, the axial spring constant (k_1) and diagonal spring constant (k_2) have the following relationship, $\mathrm{k}_1 = 2k_2$ [42]. Detailed information on the sLSM is provided in the Supplementary Information.

Figure set

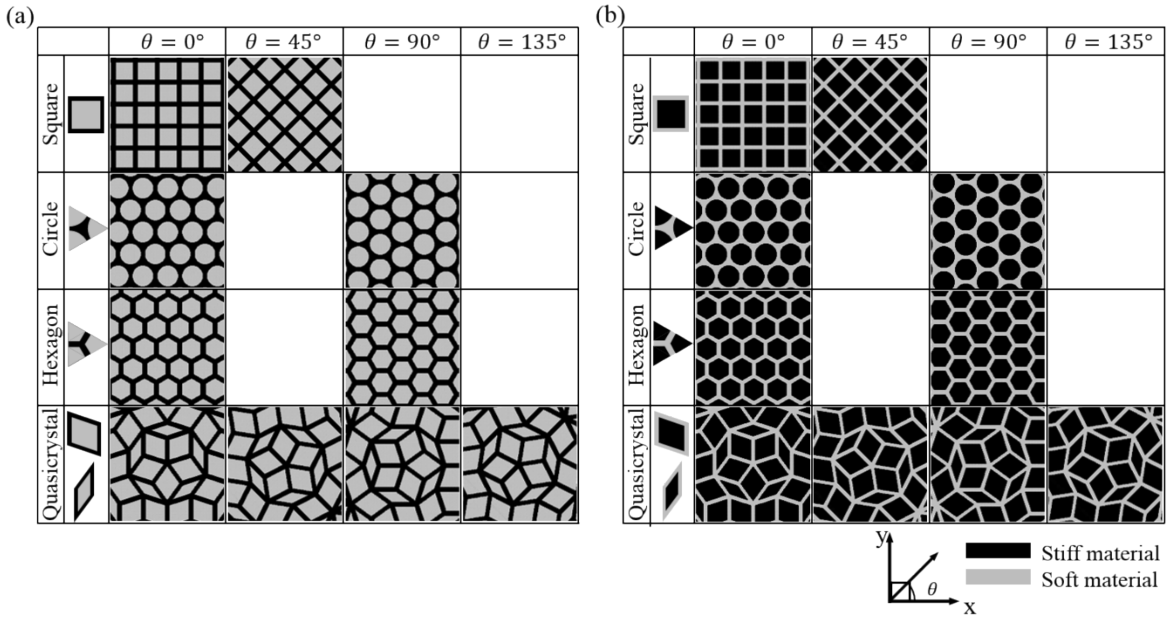

Figure 1. Schematic of the (a) soft tile stiff boundary (SoTStB) composite and (b) stiff tile soft boundary (StTSoB) composite with square, circular, hexagonal, and quasicrystal tiles and unit structures in square, triangular and quasicrystal lattices. The rotated topologies are divided into different columns (for different rotation angle), also taking into account the rotational symmetry of each structure.

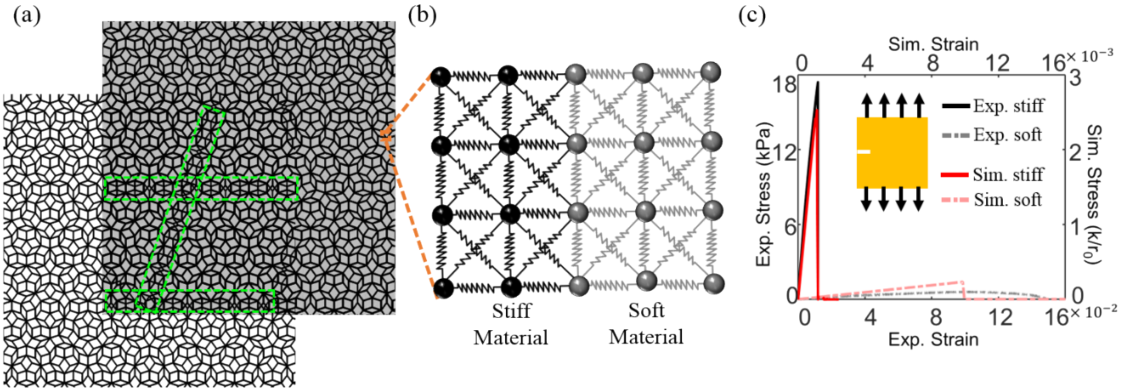

Figure 2. (a) Large quasicrystal structure composite. (b) Configuration of the adopted sLSM (square lattice spring model). (c) Numerical and experimental stress-strain curves of the homogeneous base materials: tests were carried out on square single edge-notched samples. The detailed conditions of the experimental/simulation samples are provided in the Methodology section.

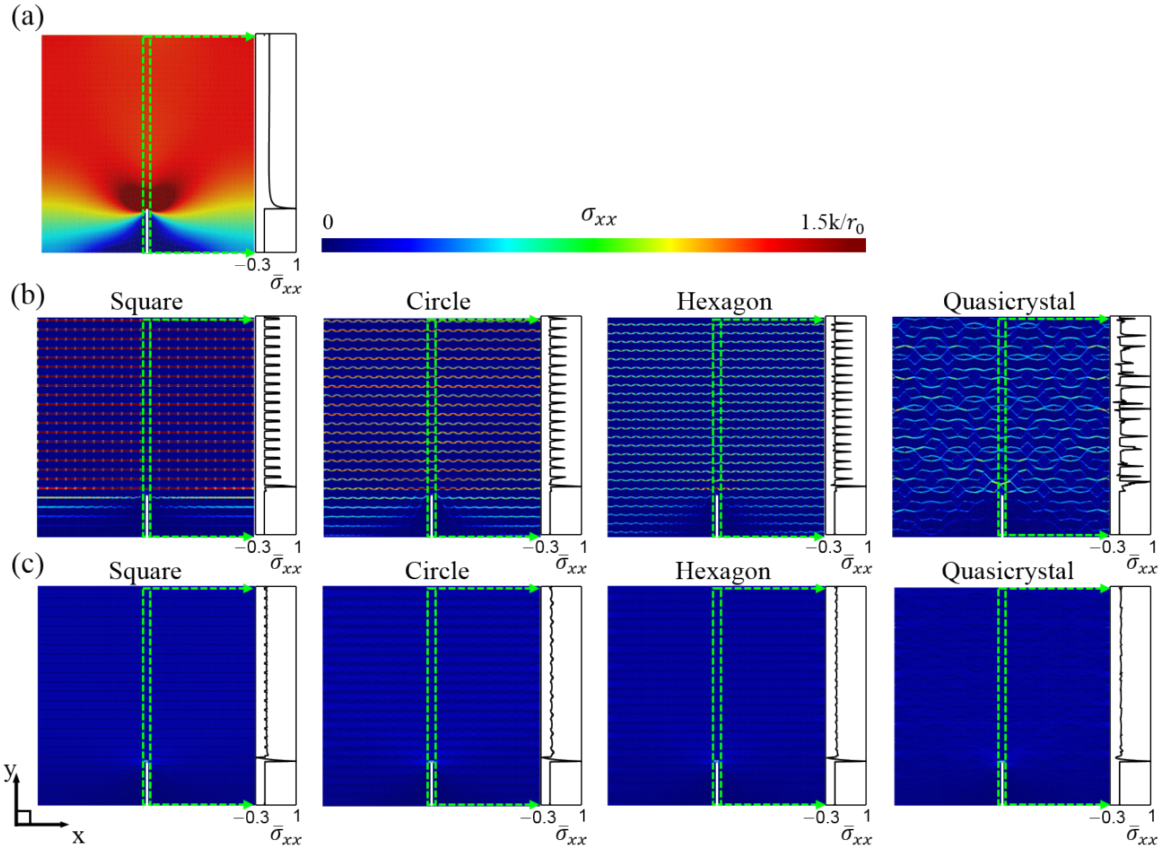

Figure 3. Stress (σ_{xx}) distribution of (a) stiff homogeneous sample, (b) SoTStB composite, and (c) StTSoB composite samples with 0° rotated topologies. The stresses of each sample were measured when the samples were subjected to uniaxial tension $\varepsilon_{xx} = 0.001$ in the simulations. The units for stress are represented as the function of the spring constants (k) and undeformed axial spring length (r_0). ($\overline{\sigma}_{xx}$) represents the averaged (σ_{xx}) in the green-line-highlighted strip, normalized by the maximum average stress in each strip. The ($\overline{\sigma}_{xx}$) trend is plotted on the right side of each graph and shows a reduction of stress concentration in the SoTStB composites. The pre-existing cracks are highlighted as thick white lines.

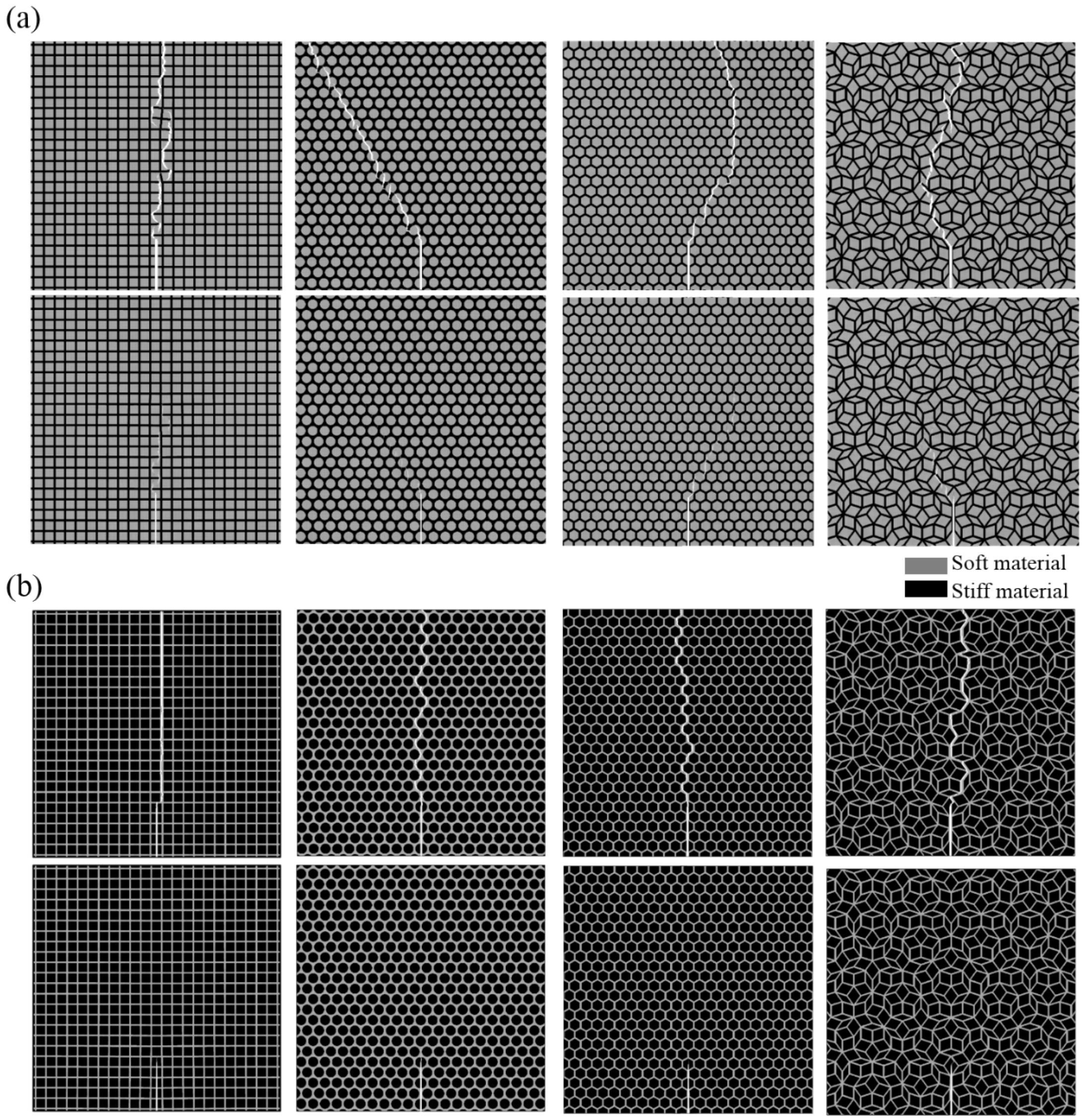

Figure 4. Snapshot of crack propagation and principal toughening mechanisms in all the samples having the 0° rotated topologies. (a) SoTStB composites: uncracked-ligament bridging, constrained microcracking, and crack deflection along the soft tile from the interactions between the crack tip and the defects ahead of the crack tip. (b) StTSoB composites: crack deflection along the soft boundary and soft boundary bridging.

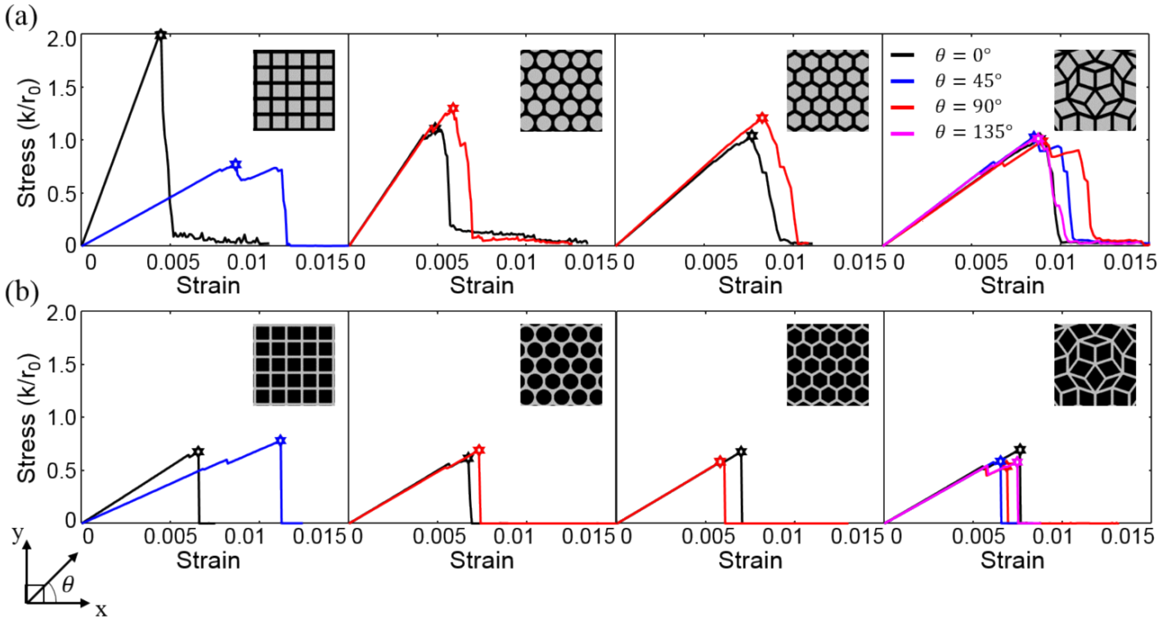

Figure 5. The stress-strain curves for the (a-d) SoTStB and (e-g) StTSoB composites with rotated topologies measured in the simulations. The maximum stress points, assumed to be the fracture initiation point, are illustrated as ‘ ⋆ ’. The units for stress are represented as a function of the spring constant (k) and undeformed axial spring length (r_0) used for the sLSM simulations.

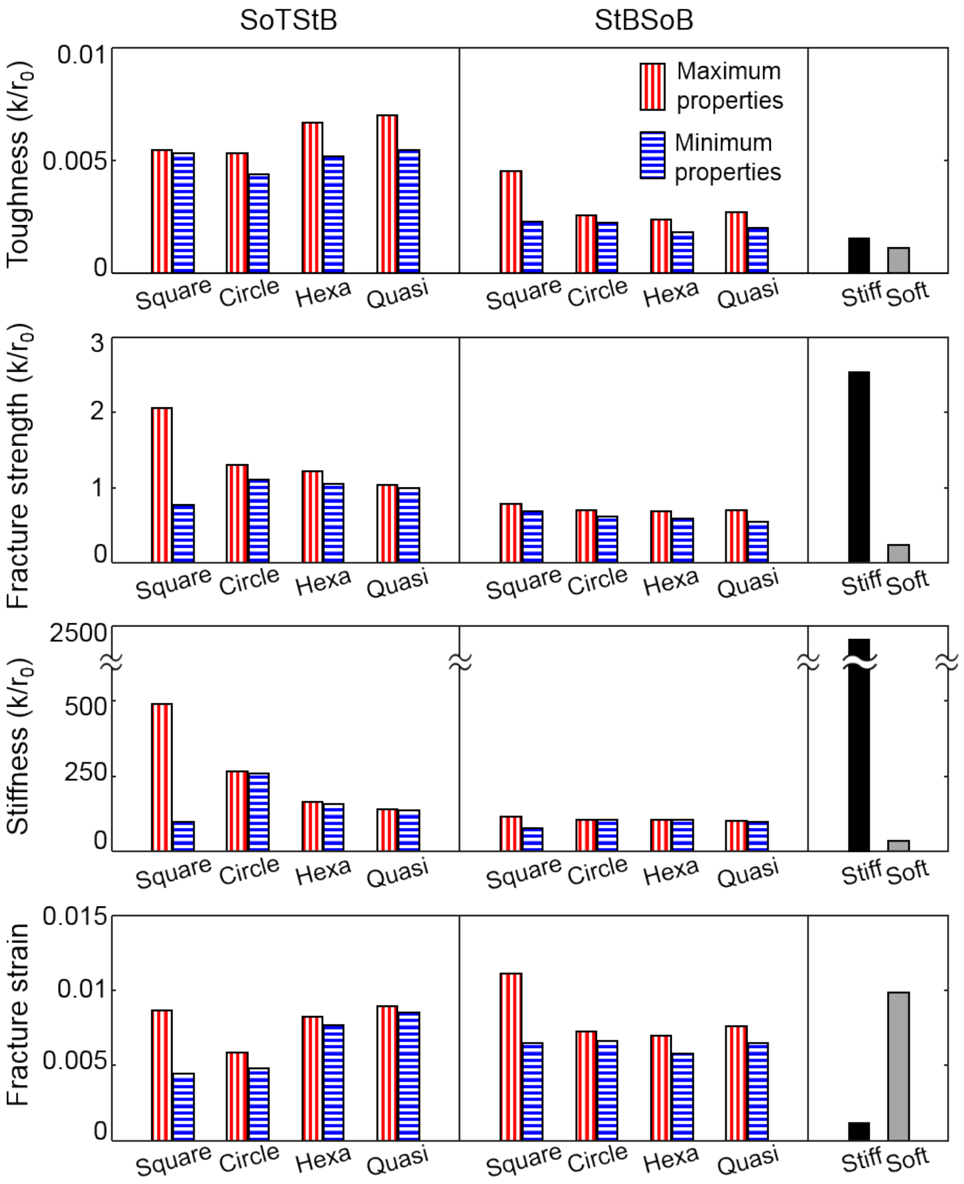

Figure 6. The maximum and minimum mechanical properties of toughness, stiffness, fracture strength, and strain measured in the uniaxial tensile simulations of the SoTStB and the StTSoB composites (containing an edge crack) by rotating the topologies. The properties are compared with the properties of homogeneous base materials and presented with the unit of spring constant (k) and undeformed axial spring length (r_0) used for the sLSM simulations.

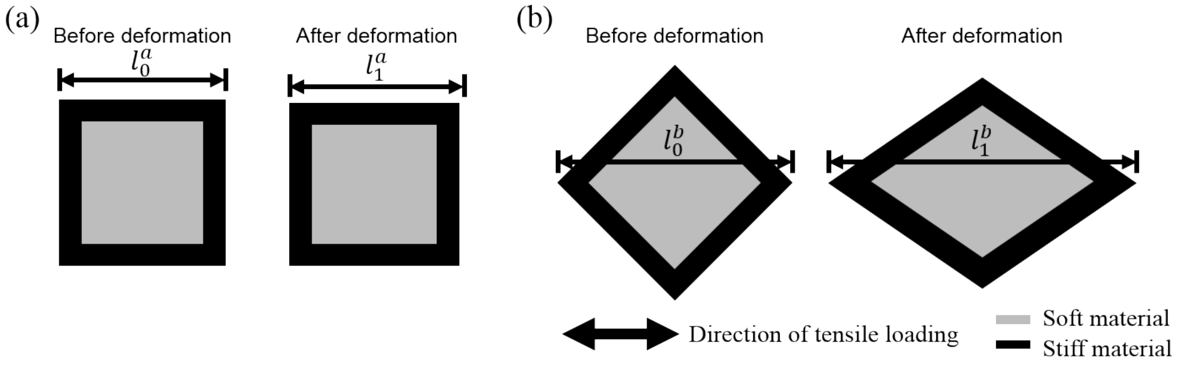

Figure 7. Schematic of the deformation mechanism of the square, circle, hexagon and quasicrystal structures with the SoTStB. In sqaure in (a) the stretching-dominant direction, having relatively small deformation, i.e. $l_0^a \approx l_1^a$ and (b) the bending-dominant direction, having large deformation, i.e. $l_0^b < l_1^b$, at a given tensile stress.

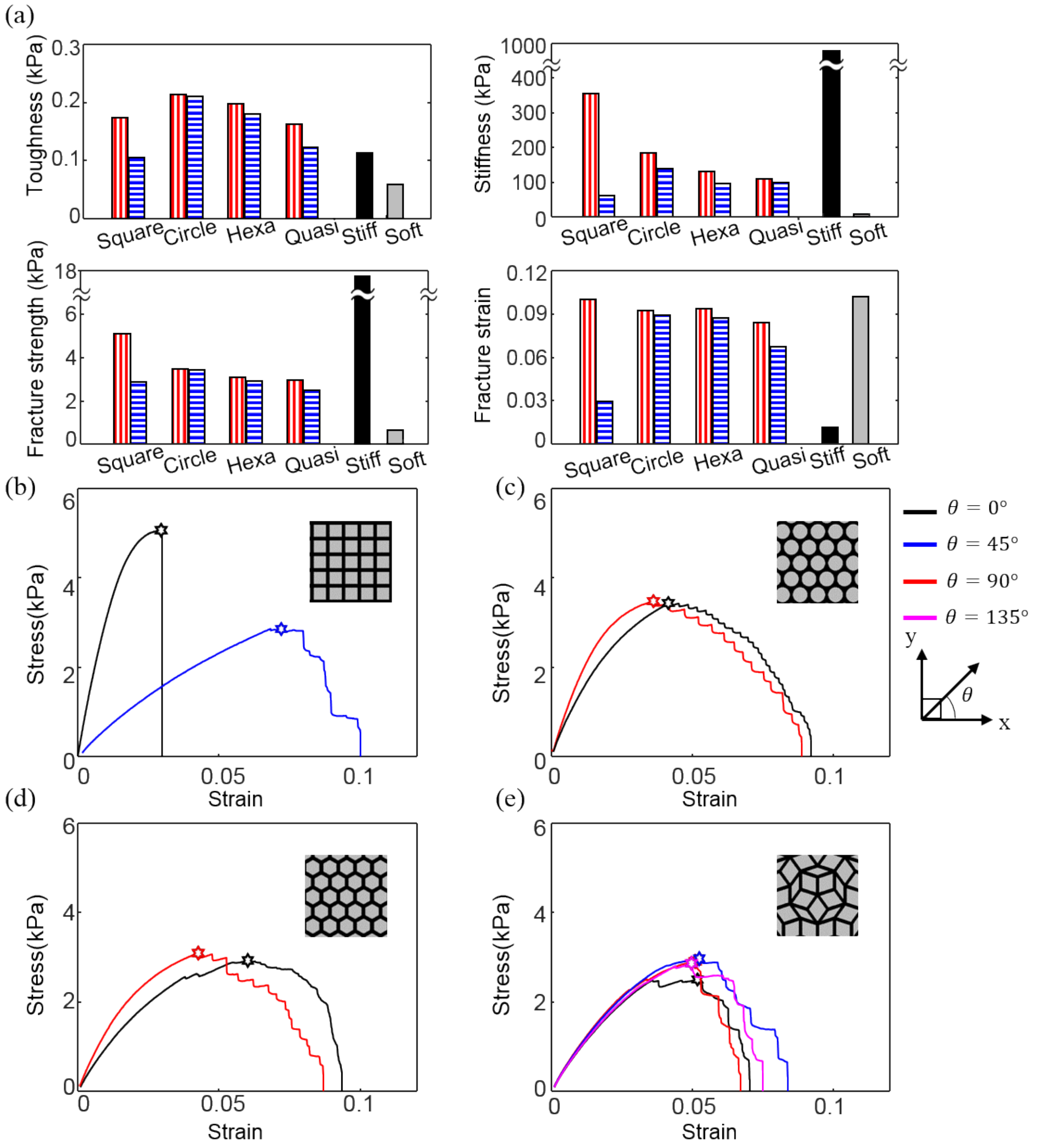

Figure 8. (a) The maximum and minimum properties of the SoTStB composites measured in the experiments. (b-e) Stress-strain curve obtained from the tensile experiments with (b) square, (c) circular, (d) hexagonal, and (e) quasicrystal composite samples. The maximum stress points, assumed to be the fracture initiation point, are illustrated as ‘ ⋆ ’.

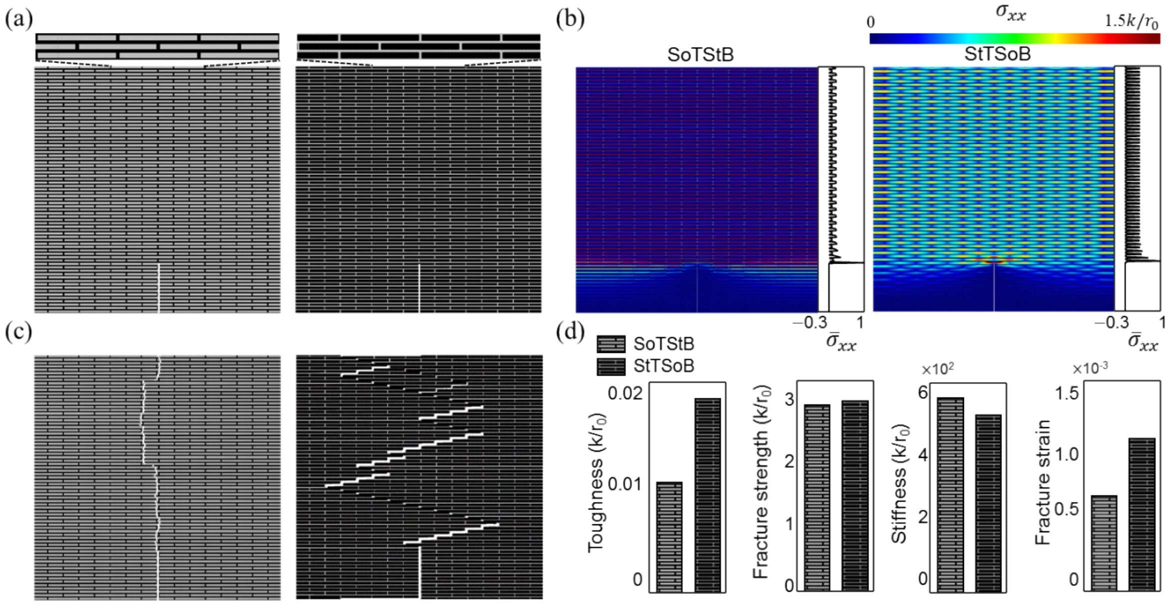

Figure 9. (a) Staggered platelet composites having the SoTStB and StTSoB. (b) The stress (σ_{xx}) distribution measured at $\varepsilon_{xx} = 0.001$ in the simulations for both cases. ($\overline{\sigma}_{xx}$) represents the average of stress component (σ_{xx}) in the green-line-highlighted strip, normalized by the maximum average stress in each strip. (c) Snapshots showing the final fracture of both samples. (d) Mechanical properties of the composites in terms of the spring constant (k) and undeformed axial spring length (r_0).

Supplementary Information

1. Defining equivalent unit cell for Penrose tiling with other structures

Unlike the square, circle and hexagon structures, which can be expanded into two-dimensional space with a periodic arrangement of single unit cells in Bravais lattices, as represented in Figure S1, Penrose tiling is composed of two different types of unit structures: a thin rhombus having an acute angle of $\pi/5$ and a thick rhombus having an acute angle of $2\pi/5$, as shown in Figure S2(a). Therefore, we have to set up specific conditions of equivalent unit cells to allow a fair comparison between the Penrose tiling and the other structures. In this work, a periodic average structure of Penrose tiling was adopted [1], and specified to have an area equivalent to that of the unit cell characteristic of other structures. The periodic average structure of the Penrose tiling with edge length, l_0, has a rhombus shape with an edge length, l^*, and an acute angle of $2\pi/5$. The geometrical relationships are the following:

$$l^* = l_0(3-\tau)/\tau \qquad \tau = (1+\sqrt{5})/2 \tag{1}$$

A schematic of the equivalent unit cell of each composite is shown in Figure S2 (b).

2. Mechanical behavior of triangular lattice spring model and square lattice spring model about uniaxial tension considering lattice symmetry

In this work, we adapted the square lattice spring model (sLSM) to simulate the mechanical properties of the composites. Since the triangular lattice spring model (tLSM) has been more widely used in the literature, we also provide a comparison between the mechanical behaviors of tLSM and those of sLSM. The tLSM is composed of one type of spring and the sLSM is composed of an axial spring and diagonal spring, as shown in Figure

S3. To simulate the isotropic materials in sLSM, we defined the behavior of the axial springs in terms of spring constant, k_1, and cutoff distance, $\mathrm{r}_{\mathrm{c}1}$, and the behavior of the diagonal springs in terms of spring constant, k_2, and cutoff distance, $\mathrm{r}_{\mathrm{c}2}$. These values were assigned so as to satisfy the following: $\mathrm{k}_1 = 2k_2$ and $\mathrm{r}_{\mathrm{c}2} = \sqrt{2}\mathrm{r}_{\mathrm{c}1}$ [2, 3]. To allow a comparison of the inherent mechanical anisotropy of each model, uniaxial tensile deformations were applied to the homogeneous sample modeled by the tLSM and the sLSM subjected to periodic boundary conditions, along different loading directions (ϕ). As depicted in Figure S3, the elastic response of the tLSM is more anisotropic than that observed in the sLSM. Figure S4 presents the orientation-dependent fracture strength (normalized with respect to the minimum strength of each model) and shows that the variance in fracture strength in the sLSM is much smaller than that of the tLSM. In addition, we can see that the mechanical responses (in both elastic and fracture regime) of the tLSM and sLSM have a 6-fold symmetry and 8-fold symmetry, respectively.

In Figure S5, the crack propagation path of homogeneous materials subjected to three-point bending were simulated by rotating the lattice structure of each model. We can see that the crack path of the sLSM is closer to the theoretical crack path than that of tLSM regardless of mesh alignment, and it was found that the sLSM was more suitable for predicting the crack path of isotropic materials. More details can be found in our previous study [2].

3. Normalized mechanical properties of each composite.

In Figures S6 and S7, to highlight the effect of the composite design, the measured mechanical properties of each composite (E_{comp}^{mea}) are normalized by the estimated mechanical properties of composites (E_{comp}^{est}) obtained from the simple rule of mixtures, i.e., $E_{comp}^{est} =$

$\rho E_{stiff} + (1 - \rho)E_{soft}$, based on the properties of the base materials (E) and the volume fraction of stiff materials (ρ). The mechanical properties of each base material, measured with single edge notched samples, are presented in Table S1. Significant improvement was found in terms of toughness, compared to the base materials.

4. Experimental samples and observation of fracture mechanism.

The dimensions of the 3D-printed samples are presented in Figure S8. The samples were printed in the z-direction to minimize deviations in mechanical properties and interfacial mixing occurring during the printing process. The fracture mechanisms of each composite sample are shown in Figure S9. The overall trend in fracture mechanism coincides with the simulations results.

References

1. Steurer, W. and T. Haibach, *The periodic average structure of particular quasicrystals.* Acta Crystallographica Section A: Foundations of Crystallography, 1999. **55**(1): p. 48-57.
2. Kim, Y., Y. Kim, and S. Ryu, *Elastic and fracture property analyses of triangular and square lattice spring models at a large deformation regime.* Journal of Mechanical Science and Technology, 2018. **32**(6): p. 2693-2706.
3. Wang, G., et al., *Hybrid lattice particle modeling: Theoretical considerations for a 2D elastic spring network for dynamic fracture simulations.* Computational Materials Science, 2009. **44**(4): p. 1126-1134.

Tables

(a)

	Toughness (k/r_0)	Stiffness (k/r_0)	Fracture strength (k/r_0)	Fracture strain
Stiff materials	1.59×10^{-3}	2.34×10^{3}	2.53	1.14×10^{-3}
Soft materials	1.16×10^{-3}	2.34×10	2.33×10^{-1}	9.85×10^{-3}

(b)

	Toughness (Pa)	Stiffness (kPa)	Fracture strength (kPa)	Fracture Strain
Stiff materials (VeroWhite plus)	1.12×10^{2}	9.57×10^{2}	1.74×10	1.18×10^{-2}
Soft materials (FLX9795-DM)	5.81×10	8.77×10^{-1}	6.07×10^{-1}	1.02×10^{-1}

Table S1. Mechanical properties of homogeneous stiff and soft materials samples in (a) the simulations and (b) the experiments. To measure the properties of the base materials, single edge notched samples were prepared.

Figures

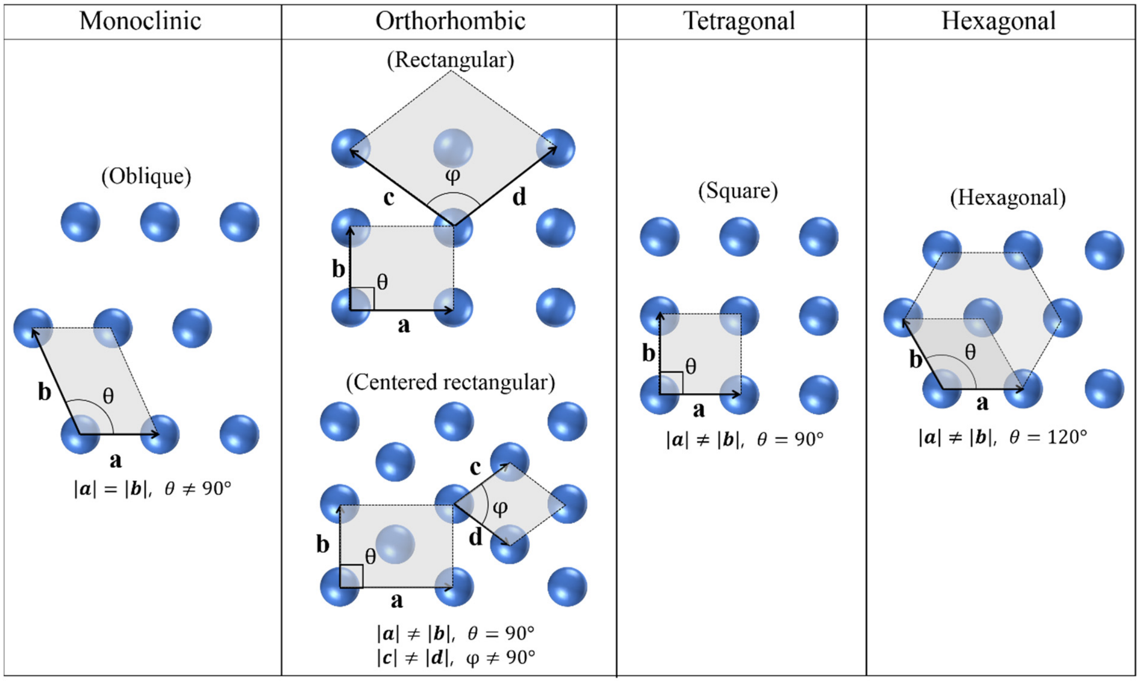

Figure S1. Schematic of five different Bravais lattices in two-dimensional space. '**a**', '**b**', '**c**' and '**d**' represent the lattice vectors and θ and φ represent the angles between them. The lattices are grouped into four crystal systems and divided into different columns. The monoclinic and orthorhombic lattices have two-fold symmetry. The tetragonal lattice and hexagonal lattice have four-fold and six-fold symmetry, respectively.

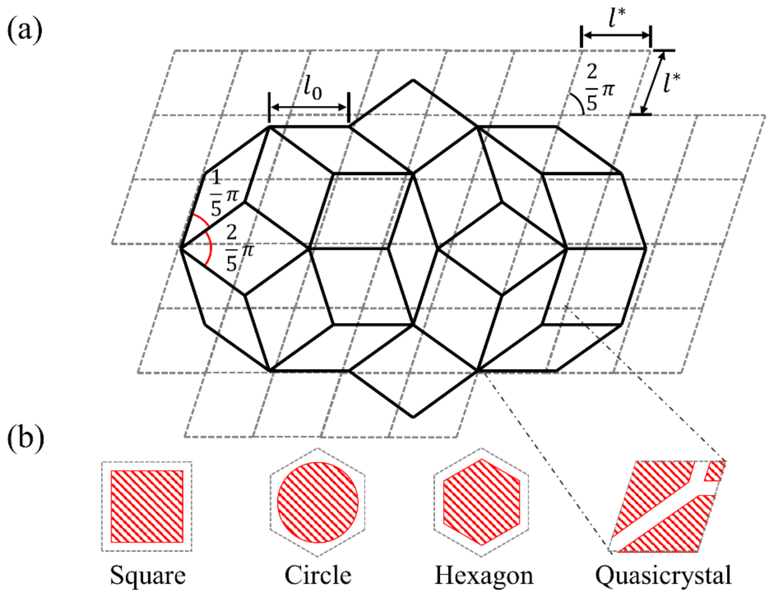

Figure S2. (a) The periodic average structure of Penrose tiling having an edge length, l^*, and an angle of $2\pi/5$ is illustrated by the gray dashed line, overlapped with the original Penrose tiling composed of thin rhombi having an acute angle of $\pi/5$ and thick rhombi having an acute angle of $2\pi/5$ with an edge length, l^*. **(b)** Unit cell of square, circle and hexagon structures in a unit lattice, and Quasicrystal averaged structure. The tile regions are hatched with red lines.

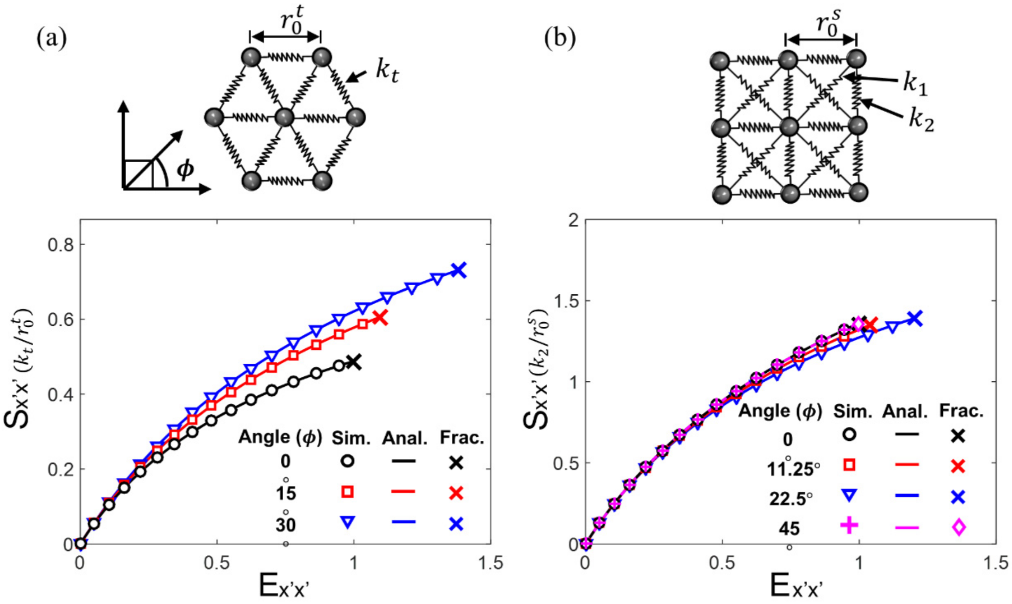

Figure S3. Stress-strain curves of homogeneous materials simulated via **(a)** tLSM and **(b)** sLSM. The plots show the outcome of uniaxial tension in the large deformation regime by varying the orientations of loading (ϕ) considering the rotational symmetry of each structure. The stress and strains are represented by the 2nd Piola-Kirchoff stress and the Green-lagrangian strain, respectively, because of the large deformation, by setting the minimum fracture strains as 100%. The units for stress are given in terms of the spring constant, for tLSM (k_t) and of the axial spring constant for sLSM (k_2).

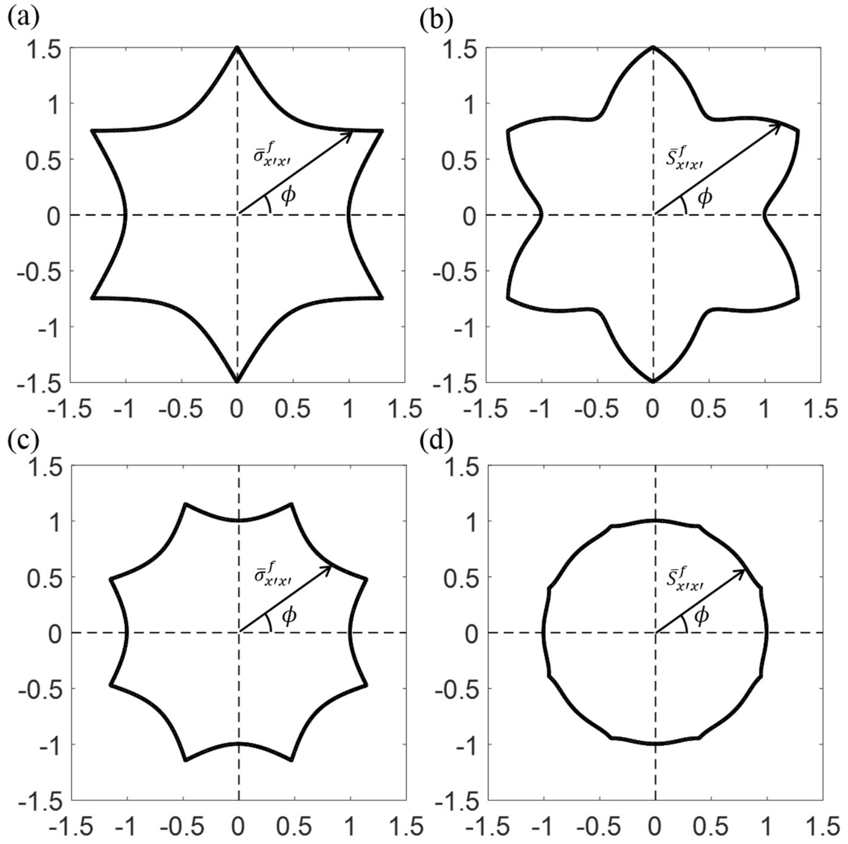

Figure S4. Normalized fracture strength $\bar{S}^f_{x'x'} = S^f_{x'x'}/\min_{\phi}(S^f_{x'x'})$ of homogeneous materials according to different orientations (ϕ) of the uniaxial tensile deformation in the infinitesimal deformation regime with **(a)** tLSM and **(b)** sLSM, and in the large deformation regime with **(c)** tLSM and **(d)** sLSM. The infinitesimal and large deformation regimes were specified by setting the minimum fracture strains at 1% and 100%, respectively. The × markers on the graph represent the simulation results. The ideal isotropic materials have an ideal circular fracture strength mapping with a radius of one, because they have constant fracture behavior, regardless of the loading direction.

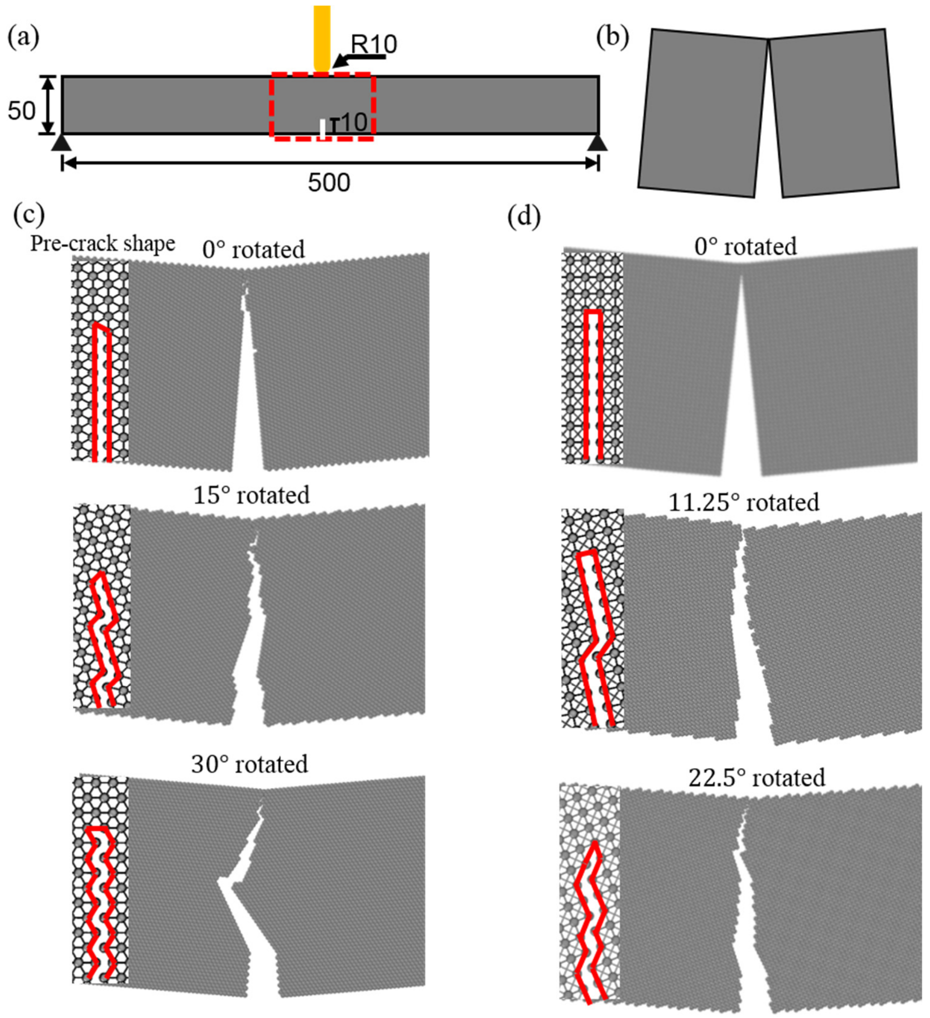

Figure S5. (a) Three-point bending simulation configurations using a rigid indenter, **(b)** Theoretical crack path of homogeneous materials for three-point bending. The simulated crack paths and the pre-crack shape for **(c)** the tLSM and **(d)** the sLSM. The red dashed line represents the magnified pre-crack shape.

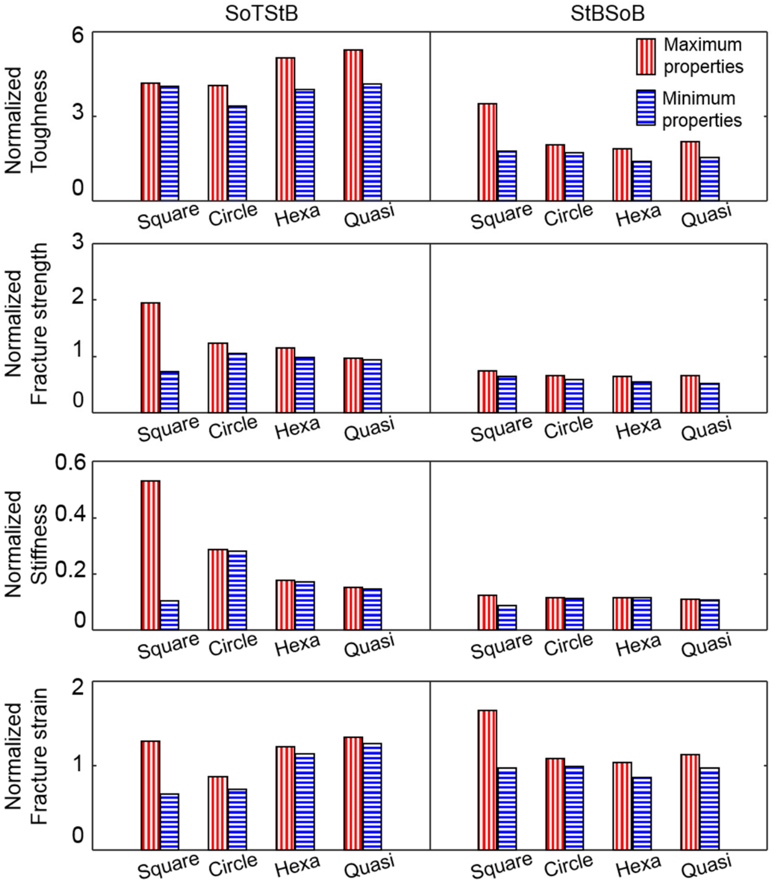

Figure S6. The normalized maximum and minimum properties of toughness, stiffness, fracture strength and strain measured in the simulations of the SoTStB and StTSoB composites. The properties are normalized by the properties of the mixture, obtained from the rule of mixtures, i.e., $E_{com} = \rho E_{hard} + (1-\rho)E_{soft}$ based on the properties of the base materials (E) and the volume fraction of stiff materials (ρ) from the simulations.

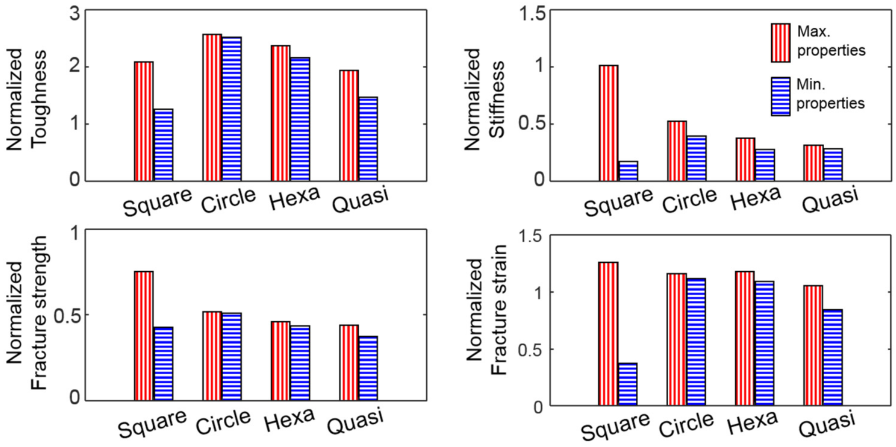

Figure S7. The normalized maximum and minimum properties of the SoTStB composites measured in the experiments. The properties are normalized by the properties of the mixture obtained from the rule of mixtures, i.e., $E_{com} = \rho E_{hard} + (1 - \rho)E_{soft}$ based on the properties of the base materials (E) and the volume fraction of stiff materials (ρ) from the experiments.

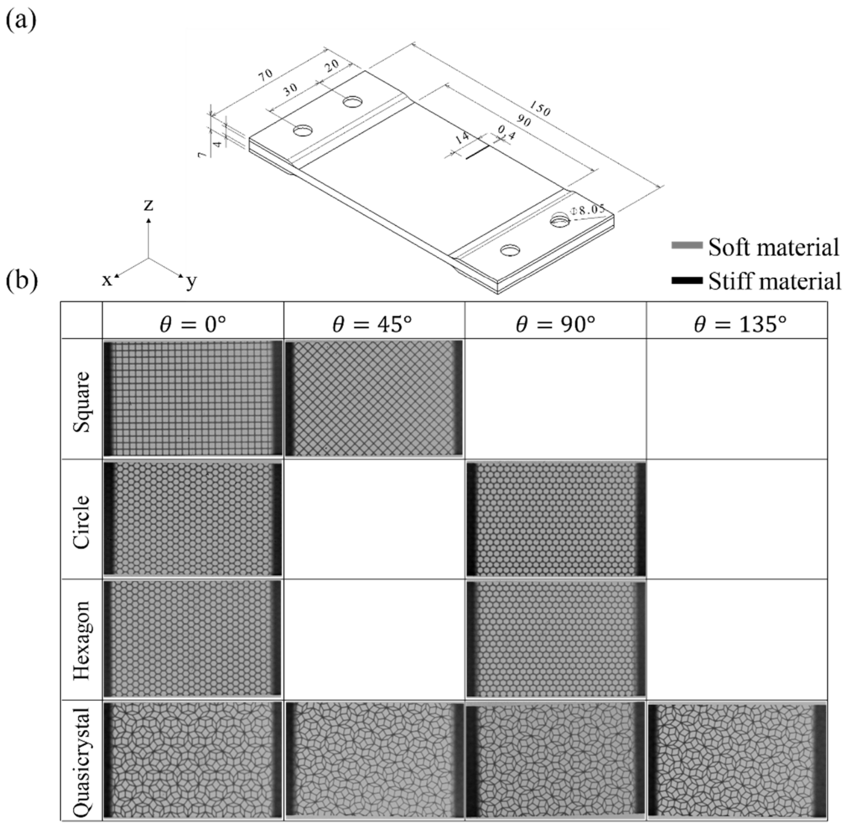

Figure S8. (a) Overall dimensions of homogenous and composite samples printed with the 3D-printer. The unit of length is millimeter. (b) The samples printed by using the 3D-printer with rotated topologies without the thickened grip part. The notch was printed and the notch tip sharpened by using a razor blade.

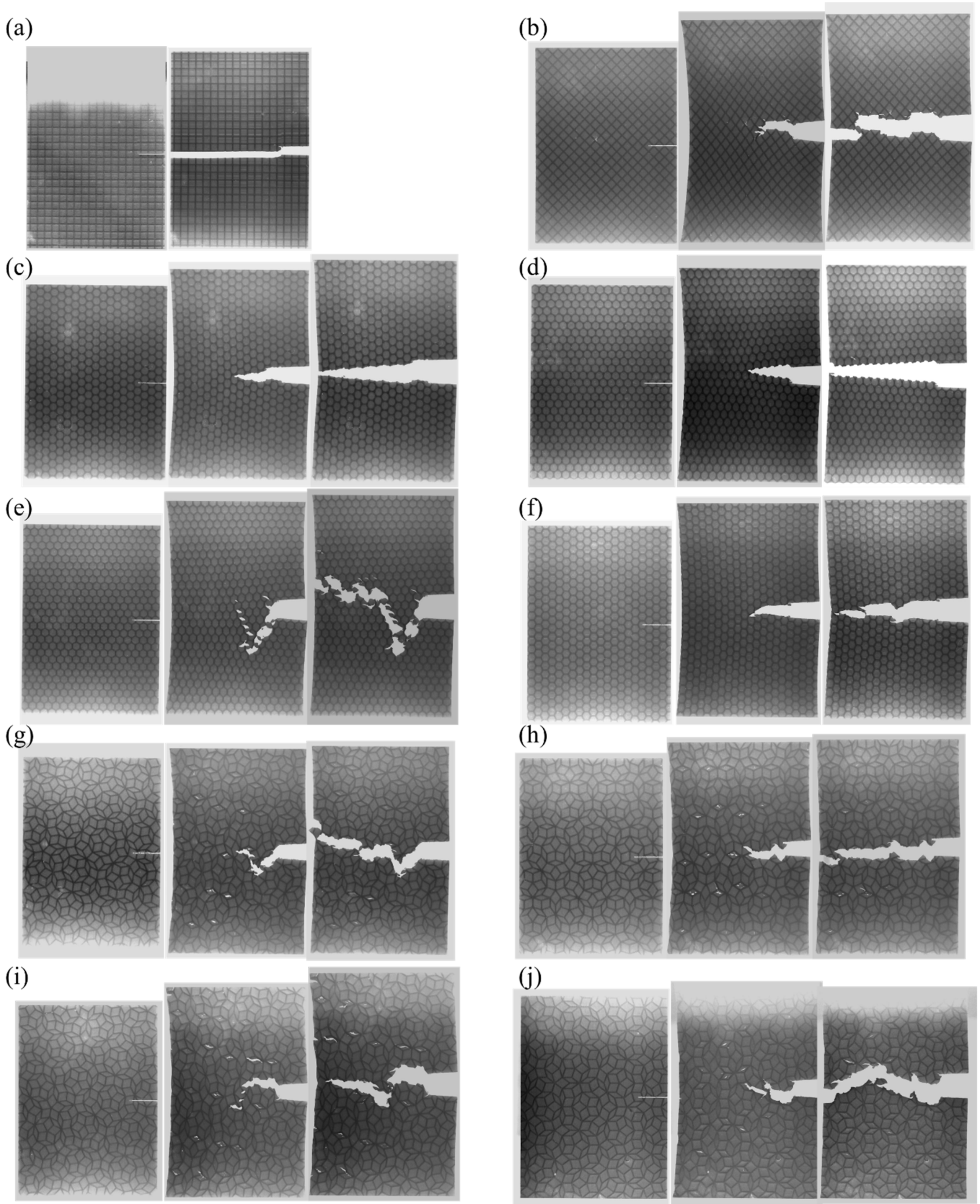

Figure S9. Snapshots of crack propagation of the SoTStB composite with (a-b) 0° and 45° rotated square topology, (c-d) 0° and 30° rotated circular topology, (e-g) 0° and 30° rotated hexagonal topology, (g-j) 0°, 45°, 90° and 135° rotated quasicrystal topology. The first snapshots of each experiment represent the initial configuration of the samples. The second snapshots were taken in the middle of crack propagation. The final snapshots were taken at the point where the tensile tester detected the fracture, with the crack almost fully propagated.